processes

MDPI

Article

CFD Simulation and Analysis of Velocity, Temperature, and Pressure Fields for Salt-Carrying Steam Flow in a U-Bend Tube

Genying Gao [1], Mingyu Luan [1], Hanzeng Cheng [2], Junde Liu [1], Yang Yang [1] and Lei Deng [2,*]

[1] Oil Production Technology Research Institute, PetroChina Xinjiang Oilfield Company, Karamay 834000, China; gaogy2@petrochian.com.cn (G.G.); luanmingyu@petrochina.com.cn (M.L.); ptrljd@petrochina.com.cn (J.L.); yangyang66@petrochina.com.cn (Y.Y.)

[2] State Key Laboratory of Multiphase Flow in Power Engineering, School of Energy and Power Engineering, Xi'an Jiaotong University, Xi'an 710049, China; chenghanzeng6@163.com

* Correspondence: leideng@mail.xjtu.edu.cn; Tel./Fax: +86-29-82668703

Abstract

To investigate the influence of salt transport in water–steam mixtures on flow and heat transfer and to ensure the operational safety of steam injection boilers, this study simulated the behavior of high-dryness steam carrying salts in U-tubes. The analysis focused on three representative substances—silica, hematite, and calcium carbonate—to evaluate their effects on flow and heat transfer characteristics under varying conditions. The simulation results show that under specified operating conditions, vortices induced by rotational flow lead to complex flow behavior in U-tubes, with transitions from stratified flow to annular flow and back to stratified flow. The effects of salt precipitation on the temperature, velocity, and pressure fields of the boiling flow were also examined. The findings indicate that for pure water, large gradients and multiple vortices adversely affect flow stability, whereas the introduction of small amounts of salts provides localized stabilization in regions of the fluid away from the wall.

Keywords: steam injection boilers; multiphase flow; salt-laden flow; U-tubes; CFD

check for updates

Academic Editor: Krzysztof Rogowski

Received: 16 September 2025
Revised: 14 October 2025
Accepted: 17 October 2025
Published: 22 October 2025

Citation: Gao, G.; Luan, M.; Cheng, H.; Liu, J.; Yang, Y.; Deng, L. CFD Simulation and Analysis of Velocity, Temperature, and Pressure Fields for Salt-Carrying Steam Flow in a U-Bend Tube. *Processes* **2025**, *13*, 3379. https://doi.org/10.3390/pr13113379

Copyright: © 2025 by the authors. Licensee MDPI, Basel, Switzerland. This article is an open access article distributed under the terms and conditions of the Creative Commons Attribution (CC BY) license (https://creativecommons.org/licenses/by/4.0/).

1. Introduction

Steam injection boilers are essential equipment in the thermal recovery of heavy oil, generating high-temperature, high-pressure steam [1,2]. This steam is injected into reservoirs through injection wells, where it vaporizes the lighter components of crude oil, thereby significantly reducing its viscosity. As a result of the combined effects of steam flooding and reservoir pressure, the de-viscosified crude is extracted to the surface through production wells [3,4]. Steam injection technology is widely employed in the extraction of heavy oil, extra-heavy oil, oil sands, and shale oil reservoirs, playing a crucial role in the petroleum industry [5].

However, steam injection boilers face challenges related to salt precipitation and deposition in feedwater, which pose significant risks to industrial safety and reduce economic efficiency [6,7]. Feedwater in conventional steam injection boilers typically contains soluble sodium salts. Given that oxygen, silicon, aluminum, iron, and calcium are the most abundant elements in the Earth's crust, their corresponding compounds are also dissolved in groundwater. To minimize costs, the reuse of groundwater increases the concentration of inorganic salts in boiler water [8]. Additionally, corrosion of boiler pipes and the addition of heavy oil extraction additives (such as silica [9] and iron oxide [10]) further raise the inorganic content. In practical applications, scale deposits are primarily composed of

silicon, iron, and calcium [11]. Inorganic salts in circulating groundwater are the direct cause of scale formation in steam boilers.

The hazards of salt precipitation can be classified into three categories: scaling, abrasion, and corrosion [12]. Salt deposits on pipeline surfaces impair heat transfer, further promoting scaling and creating a vicious cycle that may eventually lead to pipeline rupture. In the actual operations of steam injection boilers at the Liaoning Oilfield in China, pipeline ruptures have occurred due to excessively high silica content [13,14]. Even without surface precipitation, salts contribute to wear and corrosion, reducing pipeline lifespan. The accumulation of inorganic salts increases electrolyte concentration, which accelerates electrochemical reactions and promotes corrosion [15]. In conclusion, saline steam poses significant risks to the lifespan, safety, and economic efficiency of steam injection boilers [16].

Numerous studies have experimentally examined the scaling behavior in boilers [17]. Guo Feng [18] measured the solubility of calcium sulfate in solutions with various salt compositions and examined its scaling tendency in falling film evaporators under different operating conditions, providing valuable insights into the mechanisms of boiler scaling. Ammar et al. [19] investigated the effect of pretreatment processes on scaling in boiling tubes. Their experiments confirmed the necessity of water pretreatment to prevent scaling: even low concentrations of calcium and magnesium ions can precipitate under harsh operating conditions.

Salt deposition in water-steam systems and scaling patterns has been investigated. Previous studies suggest that scaling can be mitigated to some extent by adjusting temperature and pressure parameters to alter the solubility of salts. In an experimental study by Lü et al. [20] on scaling in high-salinity water within 90-degree elbows, they found that scale formation initially increased with rising flow velocity but then decreased. Once formed, scale deposits can be removed mechanically or chemically, or by ultrasonic descaling during continuous operation [21]. Zhu Jing et al. [22] used FLUENT to perform numerical simulations of calcium carbonate scaling in horizontal circular pipes. By applying the Reynolds stress model and Lagrangian method, they found that three-dimensional simulations provided significantly better results than two-dimensional simulations. Wu et al. [23] simulated scale formation in boiler water-cooled walls, comparing scale accumulation between straight pipes and bends with different angles under varying Reynolds number conditions. For obtuse-angled bends pointing downward, scale tended to accumulate on the outer surface of the bend.

Furthermore, the modeling and simulation of salt precipitation in supercritical water are currently a major research focus [24,25]. Akshay et al. [26] conducted numerical simulations of the continuous precipitation of inorganic salts in supercritical water, examining the effects of various parameters under steady-state conditions. The results indicated that temperatures above the critical temperature and the expansion of high-temperature regions in the supercritical state promote the precipitation of inorganic salts. Conversely, excessively high feed flow rates prevent the fluid from maintaining supercritical temperatures over the long term, thereby reducing salt precipitation. Zhu et al. [27] performed experimental and simulation studies on the behavior of Na_2SO_4 on heated surfaces in supercritical water. At low temperatures, the density of water is highly pressure-dependent, and salt solubility decreases significantly as the density decreases. At high temperatures, even with further reductions in density, solubility no longer decreases significantly. As a result, under low-temperature heating conditions relative to the water's critical point, Na_2SO_4 forms dense precipitates, whereas high-temperature heating conditions lead to the formation of loose structures. Li et al. [24] also used the aggregate equilibrium model to simulate the NaCl crystallization process in a supercritical water fluidized bed reactor, obtaining the

NaCl particle size distribution at both the reactor outlet and within the reactor. The results showed that the average particle size of the crystallized NaCl decreases as the supercritical water mass flow rate increases.

Current research on salt transport behavior in water-water vapor systems has primarily focused on supercritical conditions, while numerical simulations under subcritical conditions remain limited, with several areas still open for further investigation. In steam injection boilers, steam typically operates under subcritical conditions, and U-bends are high-risk zones for salt deposition and scaling. Therefore, investigating the salt-carrying behavior in water-steam mixtures within U-bends of steam injection boilers under subcritical conditions is crucial for suppressing salt precipitation, slowing the scaling process, and ensuring the safe and stable operation of the boiler.

This study selects water and steam as working fluids and uses numerical simulations to investigate the flow characteristics and behavior of different salts in the U-bends of steam injection boilers. The distribution characteristics of the velocity, temperature, and pressure fields for various salts in the U-bends are thoroughly analyzed. This research provides valuable insights for the stable operation of steam injection boilers.

2. Numerical Model

2.1. Model Construction and Mesh Generation

In the convection section of steam injection boilers, U-shaped bends function as key heat transfer components, designed to facilitate efficient thermal exchange between steam and flue gases within a compact configuration. The curved geometry not only enables flexible installation in space-constrained layouts but also enhances flow disturbance through centrifugal effects, thereby improving heat transfer performance and reducing ash accumulation. This study focuses on the U-tube in the convection section of a steam injection boiler at a Chinese oilfield. The tube has an inner diameter of 65 mm, inlet and outlet straight sections of 200 mm, and a bending radius of 150 mm. The geometric model of the U-tube is shown in Figure 1. The inlet steam dryness fraction was set to 0.75. To determine the inlet steam parameters of the U-tube, the horizontal pipe upstream of the convection section was first simulated, and its outlet steam parameters were adopted as the U-tube inlet conditions. The inlet steam parameters at the convection section were 626.402 K and 17.2 MPa.

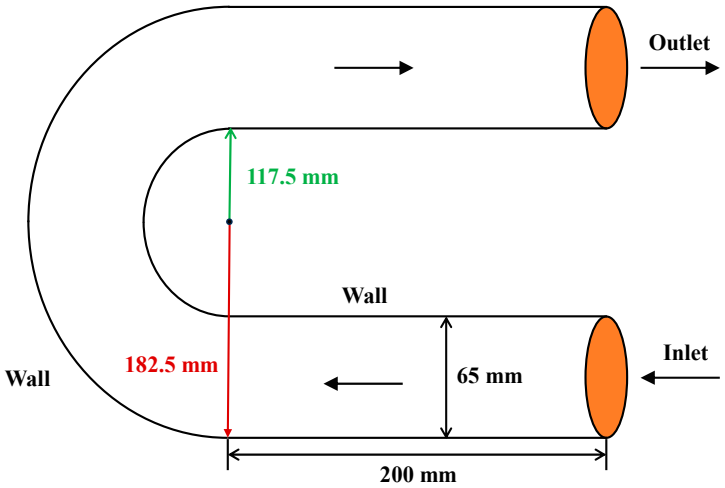


Figure 1. U-tube geometric model.

The numerical simulations in this study were performed using the commercial computational fluid dynamics (CFD) software ANSYS Fluent 2022R1. This software is a widely

used CFD tool in both industrial and academic settings for simulating complex fluid flow, heat transfer, and mass transfer processes.

For the mesh generation of regular geometries, structured hexahedral meshes were generated using ICEM to ensure mesh quality, improve computational accuracy, and enhance the stability of numerical simulations. An O-type topology was applied. At the elbow section, manual spline-type edge splits were introduced until the proportion of cells with a quality below 70% was reduced to less than 1%. The final U-tube mesh consisted of approximately 440,000 hexahedral cells. The subdivision structure is illustrated in Figure 2. Simultaneously, mesh independence verification was conducted, comparing the computational accuracy of the three meshes using maximum wall temperature and pressure drop as metrics. After comprehensively evaluating computational error and computational efficiency, the 440,000-cell mesh was selected. As shown in Table 1.

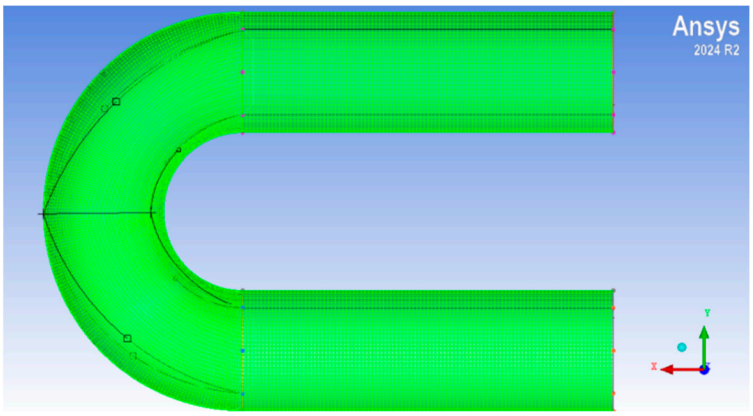


Figure 2. Top view of U-shaped pipe grid.

Table 1. Grid-independent verification.

Number of Grid Cells	Maximum Wall Temperatur/K	Error Relative to the 0.55 Million Cell Grid/%	Pressure Drop/Pa	Error Relative to the 0.55 Million Cell Grid/%
0.32 million	640.8	3.1	75.0	2.6
0.44 million	638.9	0.06	77.0	0
0.55 million	638.5	-	77.0	-

2.2. Physical-Chemical Model of Salt Dissolution

2.2.1. Salt Dissolution Model

The scale samples from the steam injection boiler were found to contain primarily silicon, iron, and calcium. Accordingly, representative salts of these elements were selected for the simulations.

For silicon, the predominant form in natural waters is metasilicic acid, which precipitates as amorphous silica or quartz crystals. In the simulations, quartz (SiO_2, cr) was selected as the solid phase owing to its low solubility and stability under operating temperatures, while orthosilicic acid tetrahydrate was chosen as the solute phase. Conventional quartz solubility equations are generally empirical, expressed in terms of variables such as water density, temperature, pressure, or salinity [28]. More recently, Andrey [29] proposed a generalized semi-empirical formulation derived from molecular dynamics and thermodynamic approaches, providing improved accuracy. According to this model, dissolved quartz in water–steam mixtures exists as monomers of protosilicic acid ($Si(OH)_4$),

dimers ($Si_2O(OH)_6$), and larger oligomers. The reaction for the monomer can be expressed as follows:

$$SiO_2(cr) + 2H_2O(l) = Si(OH)_4(aq) \quad (1)$$

$$SiO_2(cr) + 2H_2O(g) = Si(OH)_4(g) \quad (2)$$

However, the literature [30] indicates that the coordination number of metasilicic acid is 4, with a hydration number also of 4. Therefore, the reaction equation should be revised as follows:

$$SiO_2(cr) + 6H_2O(g) = Si(OH)_4 \cdot 4H_2O(g) \quad (3)$$

For iron, it primarily occurs as iron (III) oxide in steam injection boilers. The solubility of iron (III) oxide can be calculated using the Gibbs free energy method, as reported in reference [31].

$$K = \exp(-\frac{G}{RT}) \quad (4)$$

where K is equilibrium constant; G denotes gibbs free energy, J mol^{-1}; R represents gas constant, J mol^{-1} K^{-1}; T is temperature, K.

The dissolution and precipitation of ferric iron involve the following five reactions:

$$Fe^{3+}(aq) + 3H_2O(l) = 3H^+(aq) + Fe(OH)_3(s) \quad (5)$$

$$Fe(OH)^{2+}(aq) + 2H_2O(l) = 2H^+(aq) + Fe(OH)_3(s) \quad (6)$$

$$Fe(OH)_2^+(aq) + H_2O(l) = H^+(aq) + Fe(OH)_3(s) \quad (7)$$

$$Fe(OH)_3(aq) = Fe(OH)_3(s) \quad (8)$$

$$Fe(OH)_4^-(aq) + H^+(aq) = H_2O(l) + Fe(OH)_3(s) \quad (9)$$

Reference [31] provides the Gibbs free energies of various species, which allows the solubility of iron ions to be determined at specific temperatures and pH values.

In nature, at least three polymorphs of calcium carbonate exist [31]: vaterite, aragonite, and calcite. For solubility calculations, calcite—the least soluble polymorph—was selected as the representative phase. According to [32], the carbonate ion concentration was first derived from the bicarbonate concentration, and the solubility was then determined.

Finally, a user-defined function was developed to describe the dissolution–precipitation reactions of the different salts. The model employs the difference between the local and saturation concentrations as the driving force for the reaction, with bidirectional mass transfer between the fluid and solid phases represented through source terms. To capture the distinct precipitation kinetics of hematite, quartz, and calcite, specific phase transition factors are incorporated into the model for characterization.

2.2.2. Selection and Configuration of Material Properties

Most custom material properties and reaction enthalpies, except those of hydrated molecules, were obtained from the NIST database and REFPROP software 10.0. For hydrated molecules, viscosity and thermal conductivity were defined to be identical to those of liquid water, since their surface-bound water layer renders their properties comparable to water clusters. In general, the effect of these low-concentration hydrated molecules can be neglected in fluid mechanics–based simulations. The solute phases considered for quartz and hematite were orthosilicic acid tetrahydrate and ferric hydroxide trihydrate, respectively, while the dissolution and precipitation of calcium carbonate were primarily

governed by water and calcium ions. The density of hydrated molecules was calculated using the following formula:

$$R_A \cdot nH_2O = \frac{m_{mole,A} + n \cdot m_{mole,H_2O}}{V_{mole,A} + n \cdot V_{mole,H_2O}} \quad (10)$$

where $R_A \cdot nH_2O$ is hydrated molecular density, kg m^{-3}; m_{mole} denotes molar mass, kg mol^{-1}; n represents number of water molecules; V_{mole} is mole volume, m^3 mol^{-1}.

The physical parameters of different phases are shown in Tables 2–4.

Table 2. Physical parameters of the first and second phases.

Items	Gas Phase	Liquid Phase
Saturation temperature (K)	626.402	
Pressure (MPa)	17.2	
Density (kg m^{-3})	122.07	561.05
Specific heat capacity at constant pressure (kJ kg^{-1} K^{-1})	19.038	11.166
Thermal conductivity (mW m^{-1} K^{-1})	153.81	453.28
Viscosity (μPa s)	24.26	64.165
Specific enthalpy (kJ kg^{-1})	2540.4	1698.3
Latent heat (kJ kg^{-1})	842.1	
surface tension (mN m^{-1})	3.058	

Table 3. Physical parameters of the third phase.

Items	Tetrahydrate Silicate	Trihydrate Iron Hydroxide	Calcium Ion
Density (kg m^{-3})	Segmented linear	1233.96	561.05
Thermal conductivity (mW m^{-1} K^{-1})	Segmented linear	453.28	453.28
Viscosity (μPa s)	Segmented linear	64.165	64.165
Generate enthalpy (kJ mol^{-1})	−2313.604	−924.06	Value of liquid water
specific heat (kJ kg^{-1})	Segmented linear	Segmented linear	Segmented linear

Table 4. Physical parameters of the fourth phase.

Items	Quartz	Hematite	Calcium Carbonate
Density (kg m^{-3})	2670	5240	2170
Thermal conductivity (mW m^{-1} K^{-1})	1.4	2.0	1.2
Viscosity (μPa s)	1	1	1
Generate enthalpy (kJ mol^{-1})	−910.7	−825.503	−1206.87
specific heat (kJ kg^{-1})	Segmented linear	Segmented linear	Segmented linear

2.3. Model Setup and Solution Method

2.3.1. Mathematical Model

After enabling the Eulerian multiphase flow model, the available turbulence options include the two-equation *k-ε* and *k-ω* models, as well as the seven-equation Reynolds stress model. The *k-ω SST* model was selected due to its wide application in engineering problems and high predictive accuracy. This model applies the *k-ω* formulation near walls and the *k-ε* formulation in free-stream regions, thereby combining the computational efficiency of the standard *k-ε* model with the superior boundary-layer resolution of the *k-ω* model. Moreover, the *k-ω SST* model provides reliable performance in simulating corner flows. For immiscible incompressible Newtonian fluids, the conservation equations for mass, momentum, and energy within the computational domain can be simplified and ex-pressed as follows:

$$\frac{\partial \rho}{\partial t} + \left[\frac{\partial(\rho u)}{\partial x}\right] + \left[\frac{\partial(\rho v)}{\partial y}\right] + \left[\frac{\partial(\rho w)}{\partial z}\right] = 0 \quad (11)$$

where ρ is the density, kg m^{-1}; t denotes time, s; u, v, w represent velocities in the x, y, and z directions, m s^{-1}.

$$\frac{\partial\left(\rho\vec{v}\right)}{\partial t}+\nabla\cdot\left(\rho\vec{v}\vec{v}\right)=-\nabla P+\nabla\cdot\left[\mu\left(\nabla\vec{v}+\nabla\vec{v}^{T}\right)\right]+\rho g+\vec{F} \tag{12}$$

where P is the pressure on the fluid element, Pa; g denotes the gravitational body force acting on the fluid element, m s^{-2}; μ is the dynamic viscosity, kg m^{-1} s^{-1}; F represents the external body force that includes interfacial interaction forces, N m^{-3}.

$$\frac{\partial(\rho E)}{\partial t}+\nabla\cdot[\vec{v}(\rho E+P)]=\nabla\cdot(\lambda_{\text{eff}}\nabla T)+S_E \tag{13}$$

where E represents the total energy of the fluid element, which is the sum of kinetic and internal energy, J; λ_{eff} is the represents the effective thermal conductivity, W m^{-1} K^{-1}; S_E denotes the energy source term, J.

In FLUENT, multiphase flow can be modeled using the simplified mixture model, the VOF model emphasizing phase interfaces, or the Eulerian model suited for complex systems. The Eulerian multiphase model was adopted here, as it offers high flexibility despite being the most challenging to configure. Solid particles were treated as fluid-like phases, modeled as general fluids within the multiphase system. For interphase mass transfer between water and steam, evaporation–condensation was specified using the Leemodel, which characterizes boiling-driven transfer as a function of subcooling and superheating. Additionally, interfacial concentration was defined as symmetric to account for the high secondary-phase concentration [33].

2.3.2. Boundary Conditions

The inlet employs a mass flow meter. The total mass flow rate at the convection section inlet is 0.5417 kg s^{-1}. The mass flow rates for the second and fourth phases are zero. The concentration of the third phase was determined through boiler feedwater quality testing. As shown in Table 5.

Table 5. Inlet mass flow rate of the third phase.

Third Corresponding Element	Si	Fe	Ca
Elemental Mass Concentration (mg L^{-1})	56.48	0.612	0.792
Third-phase inlet mass flow rate (kg s^{-1})	8.563×10^{-5}	9.007×10^{-8}	1.071×10^{-6}

The outlet is defined as a pressure outlet, and the wall boundary condition is specified with an equivalent roughness coefficient of 0.046 mm [34]. A constant heat flux is applied as the heating condition, with the corresponding calculated values provided in the table. The wall material is set to steel. Standard initialization is employed, calculated from the inlet. For the U-tube section, which is located at the downstream end of the main pipeline, the initial steam volume fraction of the secondary phase is set to 0.95 during standard initialization to better reflect practical conditions. This configuration accelerates the inlet fluid flow at each simulation step, thereby improving computational efficiency.

2.3.3. Computational Solution

For the initial spatial discretization, a first-order upwind scheme is adopted and later switched to a second-order upwind scheme after convergence. A coupled algorithm with N-phase volume fraction coupling is applied. The pseudo-time method is enabled, and twisted surface gradient correction is activated to address mesh distortion in the U-tube.

The pseudo-time method solves steady-state problems using transient principles, providing better convergence than Courant number–based steady-state approaches.

The U-tube mesh exhibits a moderate aspect ratio, allowing the under-relaxation factors in the control options to remain at their default values. In contrast, the horizontal circular pipe mesh has a large aspect ratio, requiring adjustment of under-relaxation factors, particularly turbulence-related coefficients: the turbulent kinetic energy is set to 0.04 and the specific dissipation rate to 0.1.

In the pseudo-time method settings, the default time-stepping method is retained. For horizontal straight pipes, to offset the reduced convergence speed caused by small relaxation factors, an aggressive length-scale method is used to accelerate intermediate computations. After initialization, a conservative length-scale method is employed to obtain a stable initial flow field, after which the scheme is switched back to aggressive. The time-scale factor is kept at the default value of 1. For U-tubes, the length-scale method is set to conservative and the time-scale factor to 0.1 to account for the strong spatial variations in flow at the bend.

3. Results and Discussion

3.1. Phase Volume Fraction Distribution and Flow Patterns of Salt-Laden Steam in U-Bend Tubes

A comparative study was conducted on the effects of gravity applied along the Y-axis versus the Z-axis for three types of salts, as shown in Figure 3.

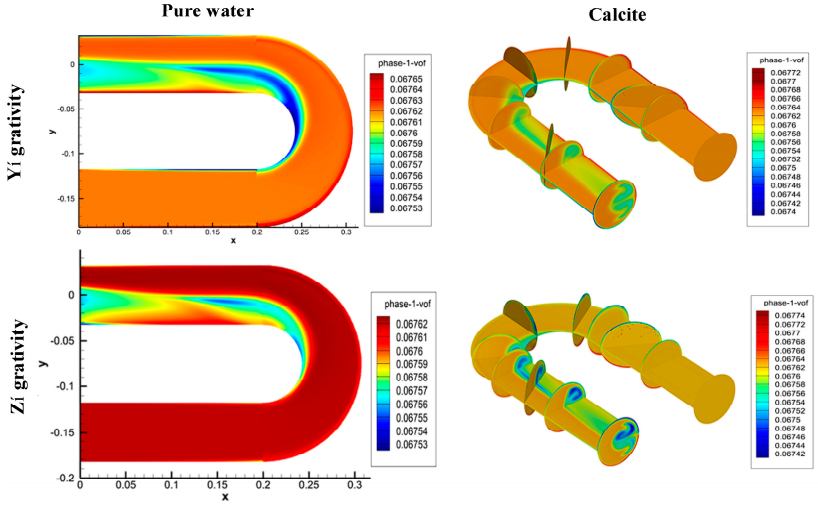


Figure 3. Liquid water phase volume fraction cloud diagram.

When gravity is applied along the Y-axis, the U-tube is oriented vertically. For pure water, the liquid phase exhibits distinct stratification along the gravitational direction, with a maximum volume fraction of 0.06765 and a minimum of 0.06753. At the straight inlet section, the lower semicircular cross-section shows a higher boundary volume fraction, indicating stratified flow induced by gravity, whereas the upper semicircular cross-section shows a lower boundary volume fraction, where boiling promotes the conversion of water into steam. As the flow passes through the elbow, the stratification tendency is disrupted. A small low-volume-fraction region develops along the inner bend, with a steep gradient in volume fraction, and the overall flow transitions toward annular flow. In the outlet straight section, stratification tends to reappear. Within the two dominant vortices at the outlet, located symmetrically on the left and right sides, the water volume fraction distributions are nearly identical.

When gravity is applied along the Z-axis, the U-tube is oriented horizontally. Similarly, distinct stratification in the liquid phase is observed, with a maximum volume fraction of

0.06762 and a minimum of 0.06753. At the inlet straight section, the lower semicircular cross-section exhibits a higher boundary volume fraction, reflecting stratified flow under gravity, while the upper semicircular cross-section shows a lower boundary volume fraction, where boiling induces vapor generation. Upon passing through the elbow, the stratified tendency is disrupted, forming a larger low-volume-fraction region on the inner bend with a sharp gradient, and the flow again transitions toward annular flow. At the outlet straight section, stratification shows signs of reemergence. However, the two major vortices near the outlet, positioned at the upper and lower regions, display distinct behaviors: the upper vortex has a smaller and more uneven water volume fraction, leading to stronger vortex structures, while the lower vortex contains a larger and more uniform water volume fraction. Under both Y-axis and Z-axis gravity, the overall water volume fraction remains relatively low, suggesting that stratified flow may be accompanied by elements of mist flow.

Taking the precipitate with the highest calcium carbonate content as an example, the effect of salt-carrying behavior on the liquid phase volume fraction is investigated. In terms of the liquid phase volume fraction distribution, salt-carrying does not significantly alter its pattern. However, as precipitated salts and solutes occupy a certain volume, salt-carrying inevitably influences the liquid phase volume fraction. Under Y-axis gravitational force, the maximum water volume fraction reaches 0.06772, while the minimum is 0.0674. Compared to pure water, the distribution range widens and the flow pattern becomes more pronounced. When gravity is applied along the Y-axis, the maximum water volume fraction increases to 0.06774, with a minimum of 0.06742. In comparison to pure water, the characteristics of the flow pattern become even more distinct.

The volume fraction distribution of hydrated molecular phases in the U-tube for different salts and gravitational orientations is shown in Figure 4. The volume fraction range for the calcium carbonate solute phase is 1×10^{-9} to 1×10^{-8}, for quartz it is 1×10^{-9} to 1×10^{-8}, and for hematite it is 1.9×10^{-8} to 2.8×10^{-8}. While steam dryness remains relatively constant, the solute phase volume fraction shows significant variation, indicating non-equilibrium local precipitation-dissolution reactions. The volume fraction distributions of the quartz and calcium carbonate solute phases, subjected to gravity along the Z-axis, follow similar patterns. From the bend to the outlet, the volume fraction changes significantly, with eddy current effects dominating over gravity. Within the eddy currents, the distribution is symmetrical, showing a distinct annular flow. The hematite solute phase, subjected to Z-axis gravity, exhibits high density, with minimal volume fraction variation from the bend to the outlet. Eddy current influence is weaker than gravity, with stratified flow being prominent. The hematite solute phase has a lower volume fraction in the upper major vortex and a higher fraction in the lower major vortex. In contrast, the flow of calcium carbonate, subjected to Y-axis gravity, shows discontinuities in solute phase distribution. At the outlet, a significant portion of the solute phase accumulates in the vortex region, resulting in a complex flow pattern.

Salt entrainment has little impact on the gas–liquid phase volume fractions, producing distributions nearly identical to those in pure water. In the straight pipe sections at the inlet and outlet, the flow of pure water approximates a mixture of mist-like and stratified flows. At the bend, the flow pattern transitions from stratified to annular flow. As the flow progresses to the outlet, vortex intensity diminishes, and the annular flow gradually reverts to stratified flow. When hydrated molecular phases experience gravitational force along the Y-axis, they exhibit stratified flow. Under Z-axis gravity, a distinct annular flow pattern forms at the outlet, with heavier water and iron hydroxide molecules tending toward stratified flow. The inorganic salt particles of the fourth phase show a strong inclination towards stratified flow. The flow pattern transition at the bend is similar to that of liquid water. After equilibrium in the dissolution-precipitation reaction, the volume fractions

of hydrated molecular and inorganic salt phases converge under low salinity conditions. Moreover, the distribution of the deposited phase is strongly correlated with the wall shear stress distribution. The simulation results reveal that in regions with higher shear stress, such as the outer side of the bend, the scouring action of the fluid on particles is more intense, effectively suppressing salt deposition. In contrast, in low-shear stress regions—such as the vortex core and the inner rear side of the bend—particles tend to adhere and accumulate, which corresponds well with the enrichment zones of the deposited phase observed in the figure.

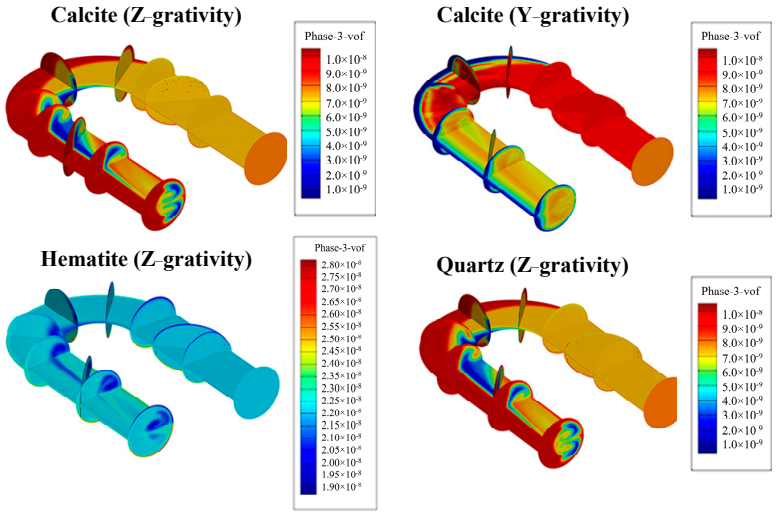


Figure 4. Hydrated molecule phase volume fraction cloud diagram.

The volume fraction distribution of sedimentation phases for different salts and gravitational orientations within the U-tube is shown in Figure 5. Under Z-axis gravity, the high density of salt particles results in minimal volume fraction variation from the bend to the outlet. The influence of vortices is weaker than that of gravity, with prominent stratified flow: the volume fraction of salt particles is lower in the upper major vortex and higher in the lower major vortex. Under Y-axis gravity, stratified flow at the outlet is less pronounced.

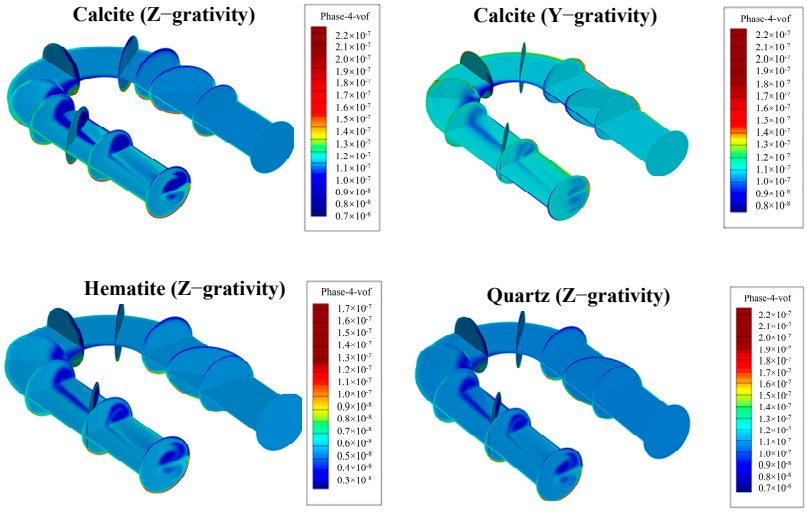


Figure 5. Sedimentary phase volume fraction cloud diagram.

In the simulation, hydrated silicate molecules under Y-axis gravity did not undergo precipitation. This may be due to the unfavorable kinetic conditions for precipitation formation, caused by the strong rotational flow, which led to the simulation terminating

upon meeting convergence criteria. The root cause, however, remains the non-equilibrium nature of local precipitation-dissolution reactions.

3.2. Velocity Field of Salt-Laden Steam Flow in U-Bend Tubes

The velocity distribution and streamlines of pure water and various salts under Z-axis gravity within a U-shaped cross-section are shown in Figure 6. The maximum velocity of the primary phase is 1.5 m s^{-1}, with a minimum of 0.1 m s^{-1}. A velocity boundary layer is clearly observed in the diagram. Starting from the mid-section of the bend, the direction of streamlines near the inner tube wall begins to change, with the flow moving progressively away from the wall until the streamlines approach and cross the central axis of the horizontal outlet pipe. For flows containing quartz, hematite, and calcium carbonate, a low-velocity region is present on the inner side at the junction between the bend and the straight outlet pipe, with nearly identical velocity distributions. Due to mesh quality effects, a numerical step discontinuity is observed in the velocity boundary layer at the junction between the outer bend and the horizontal pipe.

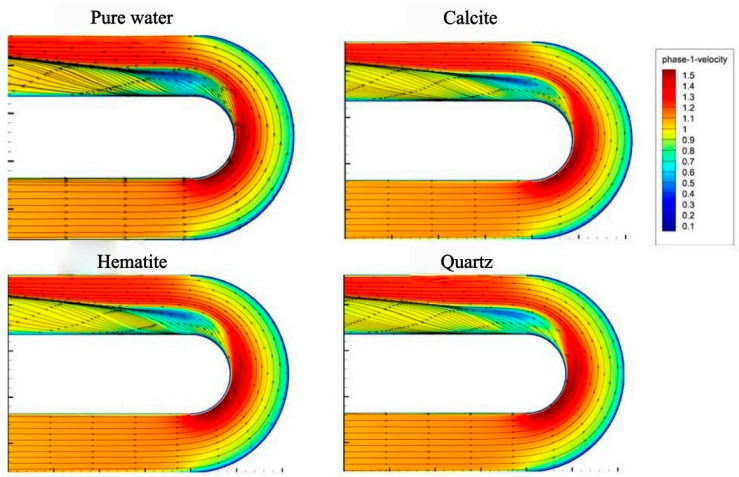


Figure 6. Z-axis velocity cloud map and streamlines under gravity.

The velocity distribution and streamlines for pure water and various salts under Y-axis gravity within a U-shaped cross-section are shown in Figure 7. The velocity distribution and streamlines under Y-axis gravity are essentially identical to those under Z-axis gravity. Additionally, for flows carrying quartz, hematite, and calcium carbonate under Y-axis gravity, the velocity field and streamline distribution closely resemble those of pure water.

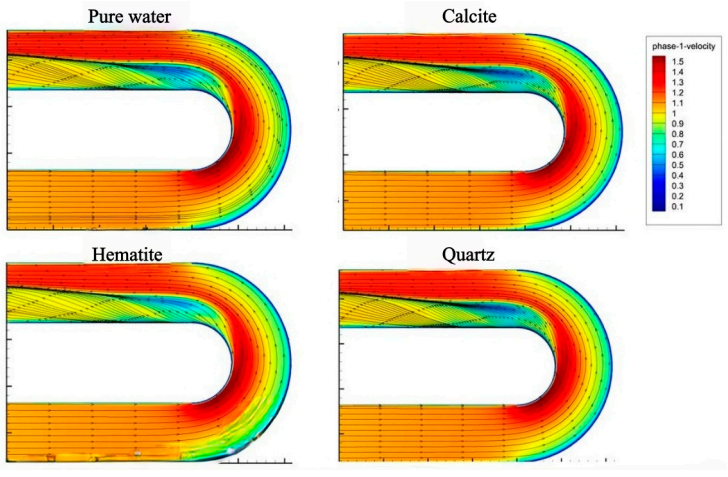


Figure 7. Y-axis velocity cloud map and streamlines under gravity.

Water carrying salts exhibits a slightly slower overall velocity compared to pure water, though this difference is minimal. This is because the water-water vapor fluid carries an insufficient amount of salts, preventing significant precipitation that could impair flow capacity in the short term. Another reason is that the inlet conditions assume a perfectly homogeneous mixture of all components, leading to insufficient stratification between the gas and liquid phases. As a result, there is no noticeable velocity slip at the phase interface, and the redistribution of velocities between the gas and liquid phases at differing speeds is not fully captured. Nevertheless, the pronounced velocity variations in the rotational flow remain unaffected by minor inlet condition variations, ensuring the reliability of the velocity results. Except when hydrated quartz and calcium carbonate molecules precipitate under Y-axis gravity, causing noticeable changes in velocity maps, the velocities across all phases remain largely consistent under other conditions. Variations in salinity and gravitational conditions have minimal impact on the velocity contour plots.

Figure 8 illustrates the velocity distribution of hydrated silicate molecules, using quartz as an example, as the third phase. The maximum velocity of the solute phase in quartz is 1.2 m s^{-1}, with a minimum of 0.1 m s^{-1}. Compared to the maximum velocity of water, the maximum velocity of the solute phase is reduced by 20%. Under Y-axis gravitational conditions, the velocity distribution of quartz's solute phase is highly non-uniform, with significant velocity gradients. Starting from the bend, the velocity of the solute phase increases, and the high-velocity region gradually expands. The maximum velocity is primarily located on the side away from the outer wall. Upon entering the straight outlet section, the high-velocity region shrinks, the overall flow velocity increases, and the maximum velocity gradually shifts closer to the outer wall.

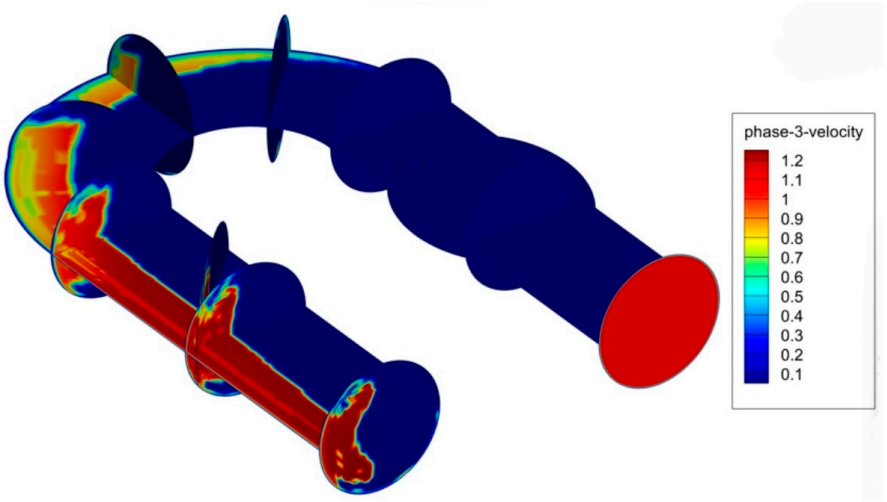


Figure 8. Velocity contour map of hydrated silica molecules under gravity on the Y-axis.

Figure 9 shows the velocity contour plots and streamlines of the liquid water phase at the outlet for pure water and high-dryness steam carrying calcium carbonate, hematite, and quartz under Z-axis gravity. The maximum velocity is 1.5 m s^{-1}, while the minimum is 0.1 m s^{-1}. The velocity distribution is consistent, with a thicker boundary layer and smaller gradient on the upper wall, and a thinner layer with a steeper gradient on the lower wall. The low-velocity region forms an umbrella-like shape, with two primary vortices symmetrically distributed along the "handle" of the low-velocity zone.

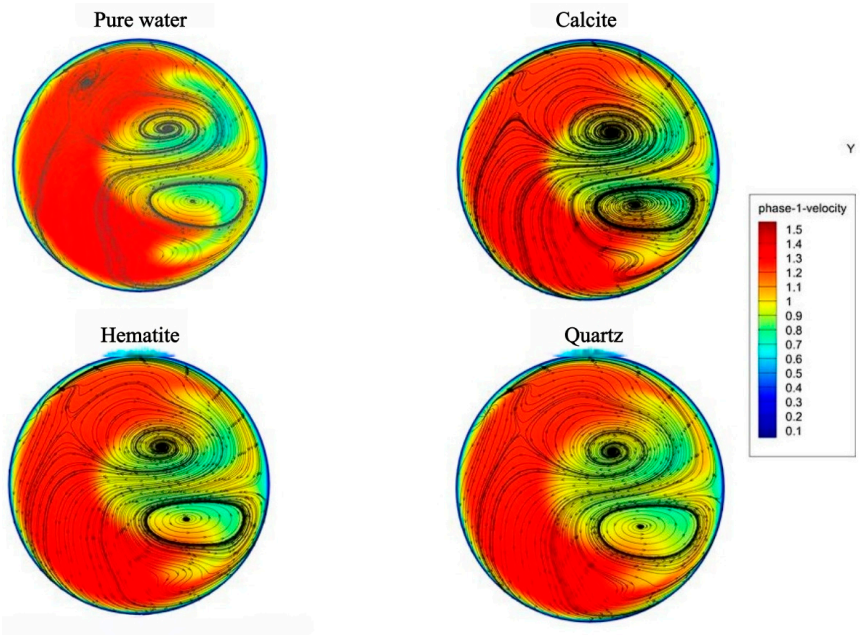


Figure 9. Z-axis exit velocity contour map and streamlines under gravity.

For pure water flow, three vortices (two large and one small) appear at the outlet. The larger vortex on the lower side is flattened and deformed, showing a distribution inconsistent with the low-velocity region, primarily due to gravity. The small vortex on the upper side can be considered a secondary vortex. In the U-tube's rotating boiling flow, vortices enhance mass and heat transfer. For flows carrying quartz and hematite, the size and distribution of vortices are similar, with two large vortices positioned one above and one below. The streamlines are sparsely distributed, clearly revealing the inflow and outflow dynamics of the two large vortices, as well as the boundary along the horizontal diameter of the circular cross-section. In the boiling flow carrying calcium carbonate, the streamlines are denser, with noticeable distortion and twisting. The upper vortex has greater intensity at its center, while the lower vortex is more intense at its periphery. The presence of salts completely suppresses the small vortices seen in the flow without salts at the outlet cross-section.

Figure 10 presents the velocity contours and streamlines of the liquid water phase at a circular cross-section 0.1 m from the outlet for pure water and high-dryness steam carrying calcium carbonate, hematite, and quartz under Z-axis gravity. The velocity contours and streamline diagrams at the 0.1 m cross-section differ from those at the outlet, with vortices exhibiting higher local relative intensity. In the salt-carrying flow, a pair of medium-sized vortices appears on the left side of the cross-section, symmetrically distributed above and below the streamline boundary. A set of small vortices forms at the lower-left corner of the large vortex on the lower right. The density of streamlines near the wall is roughly equivalent to that at the vortex edges. In the water-water vapor flow without salt, a pair of medium-sized vortices appears on the left side of the cross-section, with two small vortices forming near the wall between the medium vortices and the large vortex on the right, one above and one below.

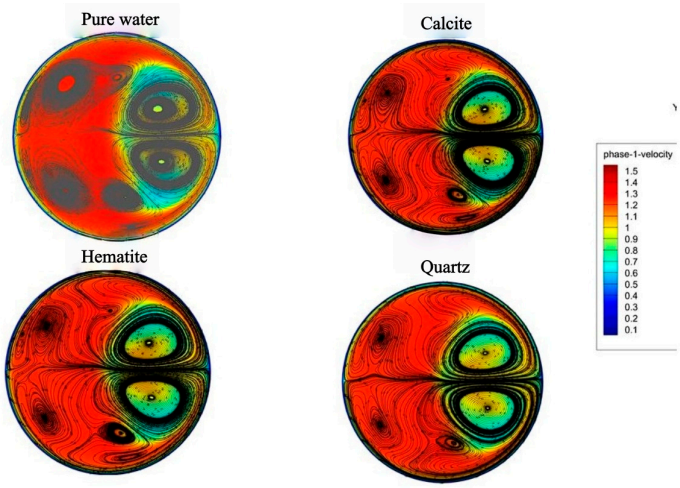


Figure 10. Z-axis velocity contour map and streamlines at a distance of 0.1 m from the outlet.

In the quartz-carrying boiling flow, only one small vortex forms. In the flows carrying hematite and calcium carbonate, two small vortices form, along with a ring of streamlines indicating the formation or dissipation of an additional small vortex. In the pure water flow, the intensity of the small vortices is relatively high, and both the medium-sized and large vortices exhibit significant intensity compared to the density of the boundary streamlines. The large vortices in the salt-carrying flow slightly extend beyond the low-velocity zone boundary, while in the pure water flow, the large vortices remain entirely confined within the low-velocity zone. In summary, under Z-axis gravity, vortices in pure water flow exhibit greater intensity, regardless of size, with small and medium-strength vortices showing higher stability and exerting stronger disruptive effects on the flow. Salt-carrying flows stabilize the large vortices by weakening vortex intensity.

Figure 11 presents the velocity contour and streamlines of the liquid water phase at the outlet for pure water and high-dryness steam carrying calcium carbonate, hematite, and quartz under Y-axis gravity. The sizes of the vortices on the left and right sides exhibit some asymmetry. Theoretically, under Y-axis gravity, the vortices on both sides should be of equal size. However, due to the use of a sampling algorithm in the streamline calculations, there are random variations in vortex size. After several iterations, the streamline diagram shown here was obtained, featuring relatively sparse local streamlines and vortices of approximately equal size.

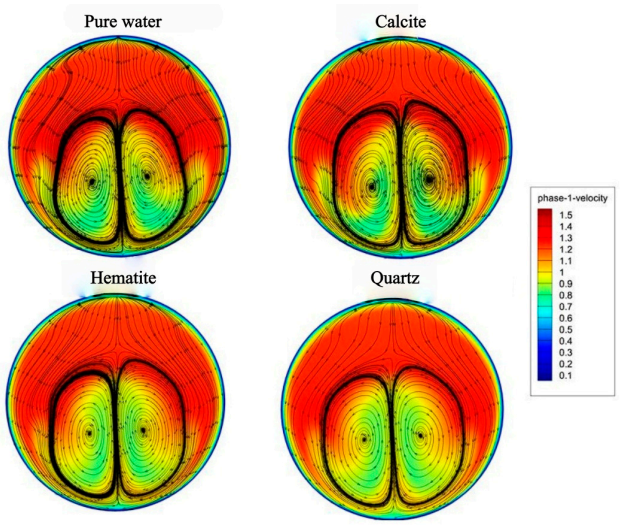


Figure 11. Y-axis exit velocity contour map and streamlines under gravity.

The vortex distribution closely matches the low-velocity flow zone. Compared to salt-carrying flows, pure water shows greater distortion in the streamlines and more turbulence in the flow. Additionally, the minimum flow velocity in the low-velocity zone is higher than that observed for the same substance under Z-axis gravity. In pure water, small vortices disappear when compared to the Z-axis gravity case. This suggests that under Y-axis gravity, the gravitational force evenly regulates the size of the two large vortices, suppressing the formation of small vortices or accelerating their disappearance.

Figure 12 shows the velocity contour and streamlines of the liquid water phase at a circular cross-section 0.1 m from the outlet for pure water and high-dryness steam carrying calcium carbonate, hematite, and quartz under Y-axis gravity. The velocity contour and streamline diagrams at the circular cross-section differ from those at the outlet, with a higher local relative intensity of vortices. Two pairs of medium-sized vortices and one pair of small vortices adjacent to the velocity boundary layer appear above the cross-section, symmetrically distributed above and below the streamline boundary. A group of small vortices forms at the upper left corner of the large vortex in the lower left region. The density of streamlines near the wall is comparable to that at the edges of the vortices.

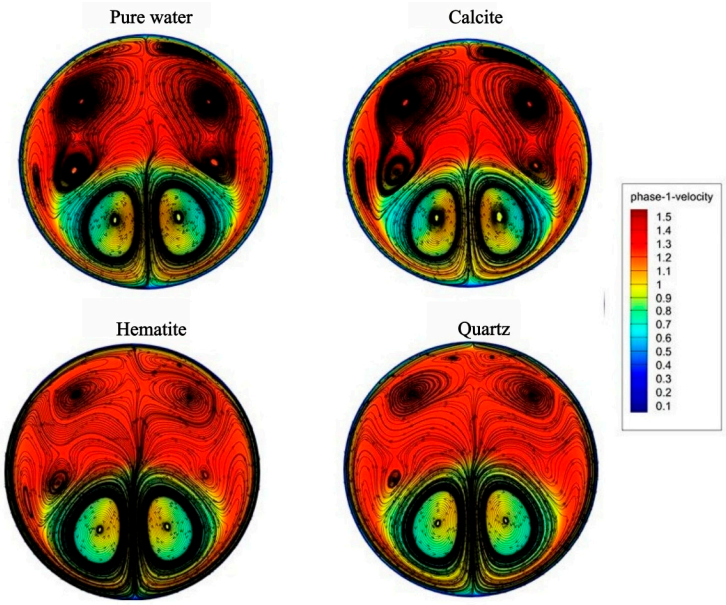


Figure 12. Y-axis velocity contour map and streamlines at a distance of 0.1 m from the outlet.

The flow carrying hematite and quartz generates and sustains vortices with lower intensity and fewer numbers. In comparison to the pure water flow under Z-axis gravity, both the intensity and number of vortices remain consistent. This confirms that under Y-axis gravity, gravitational forces evenly control the size of the two large vortices, suppressing the formation of small vortices or accelerating their disappearance.

Numerical simulation results show that carrying a small amount of salt slightly enlarges the two main vortices formed by rotational flow on the inner side of the curved pipe. It also influences the number of secondary vortices of a certain size, accelerating the merging of small and large vortices. This is because a certain concentration of salts can enhance mass transfer processes, which are influenced by the type of salt and the direction of gravity. The impact of different salts on this effect, when sediment particles are of similar size, is primarily determined by the density of the particles. For example, calcium carbonate particles, being the lightest in density, experience more sedimentation in U-tubes. However, when subjected to gravitational forces along the Y-axis, they exert

little to no influence on suppressing small vortices or promoting the development of larger vortices along the inner wall.

3.3. Temperature Field of Salt-Laden Steam Flow in U-Bend Tubes

The temperature distribution in the U-shaped cross-section of pure water and different salts under gravity along the Z-axis is shown in Figure 13. The maximum and minimum temperatures are 638 K and 627 K, respectively, and the presence of a thermal boundary layer is evident. Due to centrifugal forces, water with higher density and thermal conductivity accumulates on the outer side, while steam with lower thermal conductivity concentrates on the inner side. As a result, beginning from the mid-section of the bend, the temperature near the inner wall rises sharply. The high-temperature fluid flowing from this region gradually moves away from the wall, heating the surrounding fluid. Once it approaches and crosses the central axis of the horizontal outlet section, its temperature becomes nearly equal to that of the adjacent fluid, leading to thorough mixing of hot and cold streams. The temperature distributions of pure water and different salts are generally consistent. Combined with the velocity field results, and considering the coupling of heat and mass transfer, it can be concluded that the small amount of salt carried by high-dryness steam in the U-tube has little influence on the temperature distribution. The observed temperature profiles under Z-axis gravity for pure water and various salts further confirm this conclusion.

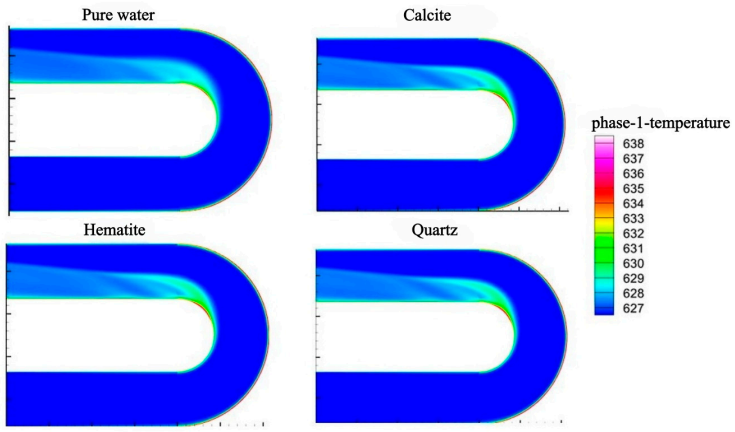


Figure 13. Z-axis temperature cloud map under gravity.

The temperature distribution across the U-shaped cross-section for pure water and various salts subjected to gravitational force along the Y-axis is shown in Figure 14. The maximum temperature reaches 639 K, while the minimum is 627 K. The temperature distribution under Y-axis gravity is essentially identical to that under Z-axis gravity. Furthermore, when subjected to Y-axis gravity, the temperature field distribution of flows carrying quartz, hematite, and calcium carbonate closely matches that of pure water. The higher maximum temperature compared to the Z-axis gravitational field indicates that fluid heating is more pronounced under Y-axis gravity, coupled with relatively greater flow resistance.

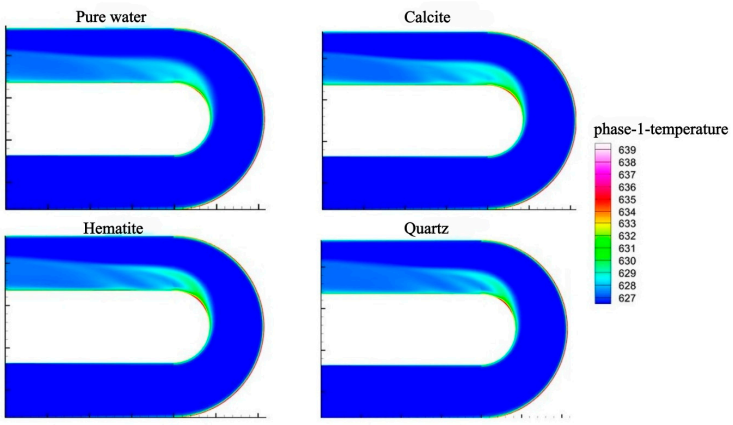


Figure 14. Y-axis temperature cloud map under gravity.

The temperature field distribution is consistent with that of the velocity field, with flow non-uniformity being the primary cause of temperature irregularities within the fluid. To more precisely assess the variations in the temperature field when high-dryness steam carries different salts, several temperature-related parameters were quantitatively evaluated, as shown in Table 6.

Table 6. Effect of salt carriage and gravity direction on maximum wall temperature.

	Items	Pure Water	Calcium Carbonate	Hematite	Quartz
Z-axis gravity	Maximum wall surface temperature/K	638.915	639.167	639.167	639.515
	Maximum wall superheat/K	12.5	12.8	12.8	13.1
	Percentage change relative to pure water/%	_	2.4	2.4	4.8
Y-axis gravity	Maximum wall surface temperature/K	639.040	639.719	639.576	639.515
	Maximum wall superheat /K	12.6	13.3	13.2	13.1
	Percentage change relative to pure water/%	_	5.6	4.8	4.0

The wall superheat of steam with 75% dryness at the inlet is approximately 13 K, with only minor variations observed due to U-tube orientation, salt type, or the presence of salts. Compared with salt-free high-dryness steam, when the U-tube is oriented horizontally, the maximum wall superheat increases by 4.8%, 2.4%, and 2.4% for quartz, hematite, and calcium carbonate, respectively. Under vertical orientation, the corresponding increases are 4.0%, 4.8%, and 5.6%. In practical operation, scaling continuously accumulates, and even a slight increase in temperature can, over long-term exposure, cause excessive wall temperatures. This may induce high-temperature creep in the pipe material, degrade its mechanical properties, or accelerate high-temperature oxidation, all of which are detrimental to the stable and safe long-term operation of the equipment.

High-dryness steam subjected to Y-axis gravity, whether carrying quartz, hematite, or calcium carbonate, generally exhibits higher maximum wall superheat than when subjected to Z-axis gravity, owing to the greater flow resistance in vertical configurations. Under Z-axis gravity, quartz yields a higher maximum wall superheat than calcium carbonate or hematite, and saline flows exceed those of salt-free steam. This is because quartz solute phases can disperse into the vapor phase, spreading across the entire cross-section and uniformly increasing flow resistance. Under Y-axis gravity, upward flow causes calcium carbonate and hematite particles to redistribute throughout the cross-section at the elbow, altering the order of maximum wall superheat from highest to lowest as follows: calcium carbonate, hematite, quartz, and pure water.

3.4. Pressure Field of Salt-Laden Steam Flow in U-Bend Tubes

Figure 15 shows the pressure distribution in the U-shaped cross-section for pure water and mixtures containing quartz, hematite, and calcium carbonate under Z-axis gravity. Due to centrifugal forces during flow, the higher-density water concentrates on the outer side, while steam accumulates on the inner side. At the bend, the pressure on the inner side is lower than on the outer side, with a significant decrease in inner-side pressure compared to the straight pipe section at the inlet. In the straight pipe section near the outlet, the pressure distribution aligns with the temperature distribution. The pressure on the inner wall surface of the outlet pipe increases, primarily due to vortex effects that cause the high-density phase to accumulate along the side walls. The streamline distribution in the outlet pipe also mirrors the pressure field distribution. The presence and type of salts primarily affect the magnitude of the pressure gradient in the outlet section, but do not significantly alter the overall pressure field distribution.

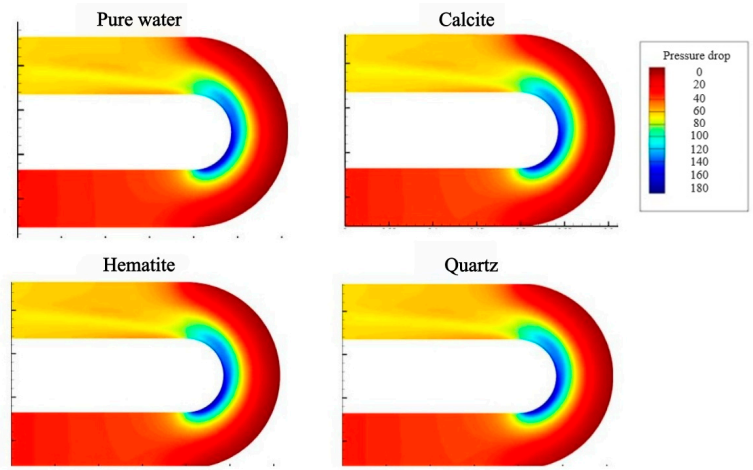


Figure 15. Z-axis pressure cloud map under gravity (The maximum value is 1.70987 × 10^7 Pa).

Figure 16 shows the pressure distribution in the U-shaped cross-section under gravity along the Y-axis for pure water and water carrying quartz, hematite, and calcium carbonate. Due to centrifugal forces during flow, the higher-density water concentrates on the outer side, while steam accumulates on the inner side. At the bend, the pressure on the inner side is lower than on the outer side, with a significant decrease in pressure compared to the straight pipe section at the inlet. In the straight pipe section near the outlet, the pressure slightly increases, primarily due to the contribution of gravitational head. The pressure on the inner wall of the outlet pipe rises, primarily as a result of gravitational effects. Pressure variations under Y-axis gravity are more pronounced than those under Z-axis gravity, and salt transport does not significantly alter the pressure distribution pattern. Due to vortex entrainment and centrifugal forces, the outer side of the elbow experiences high pressure, while the inner side shows low pressure. Similarly, the pressure distribution corresponds with the velocity and temperature distributions. To more accurately analyze the differences in the pressure field when high-dryness steam carries varying salt concentrations, several parameters related to the pressure field were quantitatively calculated, as shown in Table 7.

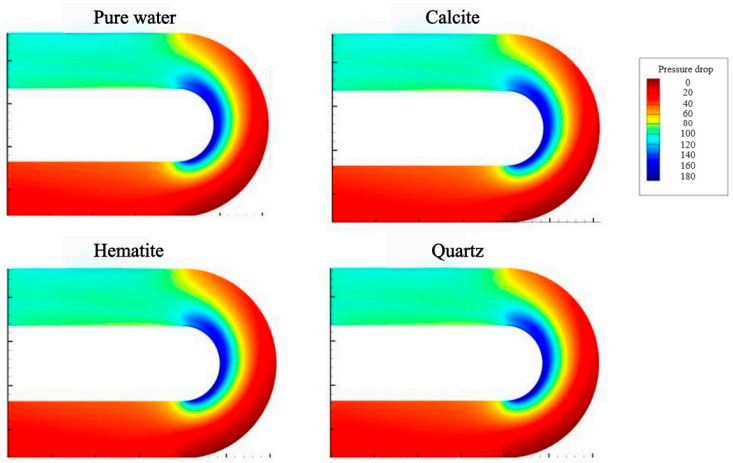


Figure 16. Y-axis pressure cloud map under gravity (The maximum value is 1.70988 × 10^7 Pa).

Table 7. The effect of salt content on gravity and pressure drop.

	Pure Water	Calcium Carbonate	Hematite	Quartz
Z-axis gravitational pressure drop (Pa)	35	21	21	21
Y-axis gravitational pressure drop (Pa)	77	77	76	34

When U-tubes are positioned horizontally, the pressure drop decreases by 40%, 40%, and 40%, respectively, for quartz, hematite, and calcium carbonate at a given concentration, compared to high-dryness steam without salt. When positioned vertically, the pressure drop decreases by 55%, 1.3%, and 0% for quartz, hematite, and calcium carbonate at a given concentration, respectively. Compared to the pressure drop in the straight pipes of the convection section, the pressure drop at the elbow significantly increases, resulting in higher flow resistance. The wear caused by salt particles in high-dryness steam is more severe at the elbow than in the horizontal pipe sections. Additionally, the maximum wall superheat increases, and the heat distribution at the elbow becomes uneven, making it more prone to safety risks due to thermal stress variations.

The pressure drop under Y-axis gravity is nearly double that under Z-axis gravity. This is because, in horizontal flow, gravity acts perpendicular to the flow direction, while in upward flow, gravity adds resistance to the flow. Salt transport significantly reduces the pressure drop in Z-axis gravity-driven flow. This effect occurs because, as shown by the comparison of velocity streamlines, hydrated molecules and solid particle precipitation effectively suppress small vortex formation, stabilizing the primary rotational flow vortex. Salt transport has a minimal effect on reducing pressure drop in Y-axis gravity-driven flow. This is due to sedimentation at the bottom of the pipe during Y-axis flow, which must shift to the opposite side, causing particle dispersion into the solution and increasing flow resistance. The larger pressure drop observed for calcite compared to hematite sediments supports this hypothesis. It can be anticipated that increased salt concentration will counterbalance the vortex-stabilizing resistance reduction with the inherent increased resistance of saline flow.

Although the presence of salts modifies the local vortex dynamics and heat transfer characteristics, the overall flow and temperature fields remain primarily governed by the water–steam mixture. This suggests that, for systems with low salinity, a computationally efficient unidirectional coupling approach could serve as a practical alternative for predicting long-term deposition behaviour. The fully coupled model adopted in this study provides a solid foundation for future validation of the reliability of such simplified methods.

4. Conclusions

This study investigated the effects of silica, iron oxide, and calcium carbonate carried by water–steam two-phase mixtures flowing through U-bends in steam injection boilers used in oilfields, focusing on their influence on boiling behavior and flow patterns. The velocity, temperature, and pressure fields under different salt-carrying conditions were systematically analyzed. The main conclusions are as follows:

(1) Under the specified operating conditions, vortices induced by rotational flow lead to complex flow behaviors in the U-bend, with flow transitions from stratified to annular flow and then back to stratified flow. Salt deposition has little effect on the overall distributions of temperature, pressure, and velocity, but markedly affects the pressure drop and maximum wall temperature.

(2) The influence of different salts on the velocity field is primarily reflected in vortex dynamics. The presence of small amounts of salts slightly enlarges the two main vortices generated by rotational flow on the inner bend and accelerates the merging of smaller vortices into larger ones. This occurs because salt addition enhances mass transfer, and the extent of this effect depends on both salt type and gravity direction. When sedimentation levels are comparable, the effect is mainly governed by salt density.

(3) The effect of salts on the temperature field is mainly reflected in wall superheating. Under Y-axis gravity, the increased resistance to upward flow results in higher wall superheat compared with Z-axis gravity. Differences among salts are primarily determined by their solubility and the distribution of particles within the flow field.

(4) The pressure drop under Y-axis gravity is greater than that under Z-axis gravity, as gravity acts against the upward flow. The addition of salts significantly reduces the pressure drop under Z-axis gravity but has a smaller effect under Y-axis gravity. The influence of different salts on pressure loss mainly depends on their solubility and the extent of particle deposition.

Author Contributions: Methodology, M.L., H.C. and Y.Y.; Software, M.L. and Y.Y.; Investigation, G.G.; Data curation, J.L.; Writing—original draft, G.G.; Writing—review and editing, M.L. and L.D.; Visualization, H.C.; Supervision, J.L. and L.D. All authors have read and agreed to the published version of the manuscript.

Funding: This work acknowledges financial support from the Research on the Characteristics of Salt Deposition in Furnace Water During the Evaporation Process of Steam-Injected Boilers and Analysis of Steam Salt-Carrying Capacity (2024XJZD09032).

Data Availability Statement: The original contributions presented in this study are included in the article. Further inquiries can be directed to the corresponding author.

Conflicts of Interest: Authors Genying Gao, Mingyu Luan, Junde Liu and Yang Yang were employed by Oil Production Technology Research Institute, PetroChina Xinjiang Oilfield Company. The remaining authors declare that the research was conducted in the absence of any commercial or financial relationships that could be construed as a potential conflict of interest.

References

1. Zhan, W. *Steam Injection Boilers for Oil Fields*; Shanghai Jiao Tong University Press: Shanghai, China, 2008.
2. Xu, Y.; Dong, B.; Dai, X. Effect of the silica-rich, oilfield-produced water with different degrees of softening on characteristics of scales in steam-injection boiler. *Desalination* **2015**, *361*, 38–45. [CrossRef]
3. Dong, X.; Liu, H.; Chen, Z.; Wu, K.; Lu, N.; Zhang, Q. Enhanced oil recovery techniques for heavy oil and oilsands reservoirs after steam injection. *Appl. Energy* **2019**, *239*, 1190–1211. [CrossRef]
4. Jun, C. *Research and Application of Condensing Oilfield Steam Injection Boilers*; Shengji Petroleum Equipment Co., Ltd., Shengli Oilfield: Dongying, China, 2021.

5. Ifticene, A.M.; Yuan, Q. Numerical modeling of in-situ hydrogen production via cyclic air-steam injection in heavy oil reservoirs. *Int. J. Hydrogen Energy* **2025**, *129*, 172–183. [CrossRef]
6. Dong, B.; Zhai, X.; Xu, Y.; Lin, S.; Zhao, W. Characteristics of Salt Deposition in Oilfield Steam Injection Pipelines. *Petrochem. Ind.* **2015**, *44*, 1524–1528.
7. Gu, J.; Lü, J.; Wu, Y.; Zhang, J.; Wu, P.; Wu, L.; Wu, W. Coal-fired Steam Injection Boiler for Superheated Steam Production Using Saline Wastewater. *Ind. Boil.* **2019**, 1–6. [CrossRef]
8. Wei, T.; Zhao, J.; Jiang, Y.; Fu, F. Technical Renovation of the Fire and Water Control Circuit for Steam Injection Boilers in Oilfields. *Pet. Chem. Equip.* **2013**, *16*, 79–81.
9. Pratama, R.A.; Babadagli, T. A review of the mechanics of heavy-oil recovery by steam injection with chemical additives. *J. Pet. Sci. Eng.* **2022**, *208*. [CrossRef]
10. Wang, H.; Fan, W.; Li, J.; Tang, X.; Qing, D.; Lu, J. Size effect of iron oxide nanocatalysts on heavy oil viscosity reduction through catalytic aquathermolysis. *J. Anal. Appl. Pyrolysis* **2025**, *186*, 106949. [CrossRef]
11. Liao, X.; Lin, T. Analysis of the Formation Mechanism and Preventive Measures of Scale Deposition in Industrial Boilers. *China Mach.* **2024**, *12*, 91–94.
12. Lü, R. Analysis of the Causes of Severe Scale Buildup in a Gas Boiler and Improvement Measures. *Spec. Equip. Saf. Technol.* **2018**, *6*, 3–6.
13. Li, K.; Fu, L. Formation and Hazards of Boiler Scale. *First Heavy Ind. Technol.* **2000**, *04*, 101–102.
14. Lu, Q.; Liu, D.; Ma, G.; Shen, L. Analysis of Pipe Burst Caused by High Salt Content in Recycled Water in Steam Boilers. *J. Liaoning Univ. Pet. Chem. Technol.* **2010**, *30*, 19–22.
15. Shen, L. *Mechanical Engineering Materials*; Xi'an Jiaotong University Press: Xi'an, China, 2023.
16. Khan, R.; Mourad, A.-H.; Wieczorowski, M.; Damjanović, D.; Pao, W.; Elsheikh, A.; Seikh, A. Erosion-corrosion failure analysis of the elbow pipe of steam distribution manifold. *Eng. Fail. Anal.* **2024**, *160*, 108177. [CrossRef]
17. Bozorgian, A.; Ghazinezhad, M. A Case Study on Causes of Scale Formation- Induced Damage in Boiler Tubes. *Biochem. Tech.* **2018**, *2*, 149–153.
18. Guo, F. *Scaling Tendency and Mechanism of Calcium Sulfate in Horizontal Tube Falling Film Evaporators*; Shandong Jianzhu University: Jinan, China, 2024.
19. Al Helal, A.; Soames, A.; Iglauer, S.; Barifcani, A.; Gubner, R. Effect of Pretreatment Process on Scale Formation in the Re-Boiler Section of Monoethylene Glycol Regeneration Plant. *IOP Conf. Ser. Mater. Sci. Eng.* **2019**, *495*, 012106. [CrossRef]
20. Lü, Y.; Lu, K.; Bai, Y.; Ma, Y.; Ren, Y. Fouling characteristics of 90° elbow in high salinity wastewater from coal chemical industry. *Chin. J. Chem. Eng.* **2021**, *35*, 143–151. [CrossRef]
21. Chen, C. *Study on the Effect of Gas Content on the Descaling Process of Gas-Liquid Two-Phase Flow Pipelines*; Tianjin University of Science and Technology: Tianjin, China, 2023.
22. Zhu, J.; Zhang, H.; Tao, H. Numerical simulation of wall-oriented deposition of calcium carbonate particles in water inside a circular pipe. *Chem. Eng.* **2013**, *41*, 58–62.
23. Wu, X.; Zheng, Y.; Wang, T.; Xie, C. Numerical simulation of scale deposition in boiler water wall with different structures. *IOP Conf. Ser. Earth Environ. Sci.* **2021**, *634*, 012058. [CrossRef]
24. Li, X.; Chen, K.; Wei, X.; Jin, H.; Wang, G.; Guo, L.; Tsotsas, E. Distribution characteristics of salt crystals in a supercritical water fluidized bed reactor with CFD-PBM coupled model. *Powder Technol.* **2023**, *420*, 118357. [CrossRef]
25. Rong, S.; Wang, R.; Xie, A.; Peng, Z.; Cao, P.; Zhang, M.; Cui, J.; Chen, Y.; Guo, L. Molecular dynamics simulation and experimental analysis of nucleation and growth mechanism of mixed inorganic salts in supercritical water. *Chem. Eng. J.* **2024**, *481*, 148597. [CrossRef]
26. Yadav, A.; Gandhi, N.; Kumar, R.; Apegaonkar, S.; Bhujade, R.; Mishra, V. Numerical modelling framework of continuous salt precipitation from super-critical water. *Sep. Sci. Technol.* **2018**, *53*, 1580–1591. [CrossRef]
27. Zhu, Q.; Li, Z.; Song, Y.; Tong, Y.; Yang, T.; Cheng, Z. Effects of Superheated Surface on the Deposition Behavior of Na_2SO_4 in Supercritical Water. *Processes* **2023**, *11*, 1779. [CrossRef]
28. Stefánsson, A.; Scott, S.W.; Bjarkadóttir, A.B.; Bravo, A.J.M.; Aðalsteinsdóttir, S.M.; Straume, E.; Lemke, K.H. Silica solubility and molecular speciation in water vapor at 400–800 °C. *Geochim. Cosmochim. Acta* **2024**, *406*, 44–56. [CrossRef]
29. Plyasunov, A.V.; Zyubina, T.S. Thermodynamic Modeling of the Solubility of Quartz in Water up to High Temperatures and Pressures. *ACS Earth Space Chem.* **2021**, *5*, 941–959. [CrossRef]
30. Exley, C.; Guerriero, G.; Lopez, X. Silicic acid: The omniscient molecule. *Sci. Total Environ.* **2019**, *665*, 432–437. [CrossRef]
31. Zhang, S.; Shi, R.; Tan, Y. Comparison of the Solubility of ZnFe2O4, Fe3O4 and Fe2O3 in High Temperature Water. *J. Solut. Chem.* **2018**, *47*, 1112–1126. [CrossRef]
32. Sharifian, R.; Wagterveld, R.M.; Digdaya, I.A.; Xiang, C.; Vermaas, D.A. Electrochemical carbon dioxide capture to close the carbon cycle. *Energy Environ. Sci.* **2020**, *14*, 781–814. [CrossRef]

33. Zhang, M. *Fluid Mechanics*; Higher Education Press: Beijing, China, 2010.
34. Tan, Z.; Cao, Z.; Chu, W.; Wang, Q. Improvement on evaporation-condensation prediction of Lee model via a temperature deviation based dynamic correction on evaporation coefficient. *Case Stud. Therm. Eng.* **2023**, *48*, 103147. [CrossRef]

Disclaimer/Publisher's Note: The statements, opinions and data contained in all publications are solely those of the individual author(s) and contributor(s) and not of MDPI and/or the editor(s). MDPI and/or the editor(s) disclaim responsibility for any injury to people or property resulting from any ideas, methods, instructions or products referred to in the content.